JOURNAL OF GEOPHYSICAL RESEARCH, VOL. 102, NO. B1, PAGES 493-505, JANUARY 10, 1997

Upper mantle velocity structure beneath the Tibetan Plateau from Pn travel time tomography

D. E. McNamara, [1,2] W. R. Walter, [3] T. J. Owens, [1] and C. J. Ammon [4]

Abstract. We inverted 1510 *P* arrival times from regional distances (333-1600 km), in and around the Tibetan Plateau to map the lateral velocity variation within the uppermost mantle. Previous studies have placed first-order constraints on upper mantle velocities but relied on data recorded almost exclusively at stations outside of the plateau. We improve resolution by using 40 events recorded at stations within the Tibetan Plateau. We combine these data with observations obtained from the International Seismological Centre (ISC) to extend our coverage by including *Pn* arrivals from 85 additional plateau events, relocated in previous studies, and recorded at stations in and around the Tibetan Plateau. We use synthetic travel time data to evaluate the resolution of our data set. The observations provide good resolution to about 1° over most of the plateau and surrounding regions. Our results show average *Pn* velocities that are about 3% lower in the northern plateau relative to the southern plateau. These variations correlate well with major tectonic features and previous geophysical observations. In the Qiangtang terrane of the northern plateau, an area known to be inefficient for *Sn* propagation, *Pn* is slow relative to both the plateau south of the Banggong-Nujiang suture and the tectonically stable Tarim basin north of the plateau. This is strong evidence for the existence of partial melt within the uppermost mantle beneath the northern Tibetan Plateau. However, when laboratory estimates of relationships between temperature, velocity, and attenuation are applied, a relatively small temperature variation (240° to 370°C) is required to explain our *Pn* velocity observations. When combined with geochemical constraints from volcanics in the northern plateau, our results strongly suggest that the mantle lid is intact beneath the northern plateau. This result would preclude tectonic models involving wholesale delamination of the mantle lithosphere in the northern Tibetan Plateau.

Introduction

The Tibetan Plateau and Himalaya and Karakoram ranges are spectacular results of the continuing collision of the northward advancing Indian continent with the southern margin of Eurasia that began at approximately 40 Ma [*Harrison et al.*, 1992; *Dewey et al.*, 1988]. Nearly 2000 km of shortening has occurred during the collision, resulting in the high elevations (5000 m) and thickened crust (60-70 km) of the Tibetan Plateau [*Molnar*, 1988]. Despite numerous geologic and geophysical studies of the region there is little agreement on the dynamic processes responsible for the plateau and surrounding ranges. Previous studies of seismic velocity structure beneath the Tibetan Plateau found convincing evidence for lateral variations of mantle properties across the plateau. Generally, mantle velocity is relatively lower and mantle attenuation is relatively higher beneath the northern portion of the plateau [*Molnar*, 1990; *Molnar and Chen*, 1984; *Brandon and Romanowicz*, 1986; *Bourjot and Romanowicz*, 1992]. Variability in upper mantle lid structure can produce significant variations in seismic phase amplitude and velocity at regional distances. For example, differences in *Sn* propagation efficiency and *Pn* velocity have been demonstrated between the northern and southern Tibetan Plateau [*McNamara et al.*, 1995; *Zhao and Xie*, 1993; *Holt and Wallace*, 1990; *Ni and Barazangi*, 1983]. Commonly, regions of inefficient *Sn* propagation coincide with relatively low *Pn* velocity [A. J. Rodgers et al., Propagation characteristics of short-period *Sn* and *Lg* in the Middle East, submitted to the *Bulletin of the Seismological Society of America*, 1996; *Beghoul et al.*, 1993; *McNamara et al.*, 1995]. Lateral variations in *Pn* velocity and *Sn* propagation efficiency also have been associated with differences in upper mantle composition, temperatures and pressures [*Gajewski et al.*, 1990; *Hearn*, 1984; *Beghoul et al.*, 1993; *Hearn et al.*, 1991].

To better map the regional variations of *Pn* velocity within the Tibetan Plateau, we have inverted over 1500 travel times from 128 relocated regional events ($3° \leq \Delta \leq 16°$) (Table 1) for the lateral velocity structure within the uppermost mantle beneath the Tibetan Plateau. Our experiment is unique in that we have 11 stations located within the boundaries of the plateau (for experiment details, see *Owens et al.* [1993]) enabling us to increase the density of ray path coverage within Tibetan Plateau, relative to previous studies. The portable station data were supplemented with arrivals recorded at 69 additional International Seismological Centre (ISC) stations within the region (Table 2) (Figure 1).

[1]Department of Geological Sciences, University of South Carolina, Columbia.
[2]Now at Geophysics and Global Security, Lawrence Livermore National Laboratory, Livermore, California.
[3]Geophysics and Global Security, Lawrence Livermore National Laboratory, Livermore, California.
[4]Department of Earth and Atmospheric Sciences, St. Louis University, St. Louis, Missouri.

Paper number 96JB02112.
0148-0227/97/96JB-02112$09 00

Table 1. Tibetan Plateau Experiment Station Locations

Station	Latitude N°	Longitude E°	Elevation m
AMDO*	32.247	91.688	4712
BUDO*	35.529	93.910	4660
ERDO*	34.520	92.707	4623
GANZ*	29.767	94.050	3150
LHSA*	29.702	91.128	3700
SANG*	31.024	91.700	4740
TUNL*	36.199	94.815	3133
WNDO*	33.448	91.904	4865
XIGA*	29.234	88.851	3865
MAQI*	34.478	100.249	3823
USHU*	33.011	97.015	3727
AAA	43.271	76.947	800
AAB	43.271	76.947	134
AJM	26.466	74.650	0
ANR	40.755	72.360	494
BHK	31.416	76.417	410
BMI	27.300	92.200	2700
BRCI	27.56	81.580	123
BTO	40.598	110.018	1120
CD2	30.910	103.758	628
CDU	30.660	104.011	506
CEP	33.824	71.909	1376
CHA	26.833	87.167	161
CHCP	33.658	73.260	579
CPA	32.980	71.424	335
DDI	30.317	78.051	682
DMN	27.609	85.106	2225
DRP	31.744	70.203	638
DSH	38.558	68.775	847
FRU	42.833	74.617	655
GAR	39.000	70.317	1300
GKN	28.003	84.637	1478
GTA	39.400	99.800	1341
GUN	27.910	85.879	2900
GWH	26.100	91.467	0
GYA	26.459	106.664	1162
HMNA	25.923	92.610	0
INR	27.050	93.283	0
JHI	26.733	94.167	84
JMU	32.717	74.900	0
KAAO	34.540	69.0432	1920
KBL	34.540	69.043	1920
KHM	25.651	94.068	1630
KHO	37.483	71.533	1850
KKN	27.784	85.268	1920
KKR	29.951	76.817	257
KMI	25.123	102.740	1945
KOI	26.983	95.500	785
KRD	43.383	75.050	900
KSH	39.450	75.968	1286
KUL	37.900	69.750	605
LAH	31.550	74.333	210
LSA	29.700	91.150	3658
LZH	36.084	103.834	1560
MNL	33.135	73.750	436
NDI	28.683	77.217	230
NIL	33.650	73.250	536
NRN	41.433	76.000	2849
PKI	27.571	85.409	2758
PRZ	42.333	78.400	1599
PSH	33.937	71.434	456
PTH	29.550	80.217	1669
QUE	30.188	66.950	1721
SAM	39.673	66.990	704
SARP	31.922	72.670	183
SBDP	32.300	70.800	1356
SHL	25.567	91.883	1600
SRNI	33.95	74.750	0
TAS	41.325	69.295	470
THW	32.794	71.743	533
TLG	43.267	77.383	850
TOC	26.750	94.767	87
TURI	25.550	90.333	305
TURX	41.733	69.650	0
TZR	26.633	92.800	0
VAR	25.300	83.017	88
WMQ	43.821	87.695	970
WRS	34.150	71.401	343
XAN	34.034	108.917	630
YYI	26.567	94.683	707

* Portable stations [*Owens et al.*, 1993].

We begin with a discussion of the data selection criteria since data quality is critical to accurately estimate *Pn* velocity variations. We then describe the backprojection methods and investigate data resolution. First, we employ a tomographic inversion technique after *Hearn* [1984] that is an expanded form of the time term method of refraction [*Scheidegger and Willmore,* 1957]. We assume that *Pn* propagates through the uppermost mantle as a head wave. Travel times are modeled assuming a three-leg travel path for *Pn*. Crustal delays are computed along with lateral slowness variations within the mantle lid. Next, we examine the resolution of the data set. Finally, we discuss the relationship of the results to the regional tectonic framework. In general, regional variations in uppermost mantle velocity follow regional structural trends and likely reflect thermal and compositional variations beneath the Tibetan Plateau.

Table 2. Tibetan Plateau Experiment Regional Events

Event ID	Latitude °N	Longitude °E	Depth, km	m_b	Number of Stations
RA01	39.420	94.830	4	4.8	16
RA02	30.390	94.810	5	4.7	21
RA03	30.340	94.820	15	4.6	20
RA04	30.370	94.810	5	4.6	19
RA05	33.870	92.190	10	4.8	21
RA06	34.200	92.000	15	3.3	14
RA07	34.570	97.190	27	4.3	16
RA08	37.410	95.380	12	5.3	24
RA09	36.590	98.590	6	4.6	19
RA10	28.840	95.000	4	4.7	25
RA11	36.180	100.060	15	5.4	20
RA12	34.650	98.880	6	4.5	16
RA13	37.790	101.400	9	5.2	18
RA14	34.017	88.832	6	4.4	7
RA15	33.919	88.746	6	4.1	7
RA16	34.073	94.247	19	4.3	5
RA17	32.090	94.694	10	4.4	4
RA18	29.543	81.632	20	5.6	10
RA19	33.976	88.840	6	5.1	7
RA20	29.970	93.928	10	4.8	8
RA21	33.990	88.904	6	4.6	6
RA22	33.917	88.863	6	5.2	6
RA23	33.966	88.942	7	5.0	7
RA24	30.003	92.544	10	4.4	4
RA25	30.657	99.571	11	4.5	9
RA26	33.940	88.850	5	4.6	20
RA27	39.670	98.340	16	5.4	12
RA28	34.550	93.160	5	4.0	15
RA29	34.450	93.260	7	4.9	19
RA30	29.610	95.640	5	5.5	21
RA31	29.640	95.680	7	4.9	19
RA32	29.650	95.630	5	4.5	13
RA33	34.300	86.270	7	4.4	25
RA34	28.120	87.960	5	4.9	16
RA35	31.950	88.310	4	4.4	26
RA36	36.090	92.560	7	4.0	18

Table 2. (continued)

Event ID	Latitude °N	Longitude °E	Depth, km	m_b	Number of Stations
RA37	26.990	92.110	7	4.5	15
RA38	36.190	100.090	14	4.8	16
RA39	33.900	88.910	7	4.5	10
RA40	38.330	99.450	5	4.8	11
M03	36.950	95.500	10	5.9	2
M04	29.960	80.460	18	5.8	9
M05	28.040	93.750	15	5.9	2
M06	27.400	87.840	15	5.8	4
M07	31.490	80.500	8	6.0	8
M08	29.620	80.830	15	6.0	10
M09	28.670	78.930	20	5.6	10
M10	36.450	87.430	8	5.2	11
M11	29.620	80.790	12	5.7	13
M12	33.630	75.330	10	5.5	14
M13	28.410	94.290	15	5.7	1
M14	31.610	100.260	8	6.1	1
M15	31.570	100.310	10	5.2	1
M16	27.400	93.960	10	5.4	2
M17	30.610	103.050	7	5.8	1
M18	35.460	98.040	7	5.7	1
M19	32.160	94.990	9	5.6	1
M20	30.790	84.330	8	5.3	11
M21	32.360	92.110	8	5.5	2
M22	31.380	91.410	8	5.4	7
M23	36.650	96.350	15	5.5	1
M24	36.560	96.350	19	5.5	2
M25	35.940	73.330	12	6.2	13
M27	31.500	100.330	10	5.9	1
M28	35.160	86.400	6	5.9	17
M29	35.210	86.540	7	5.7	14
M30	32.940	104.020	4	5.5	1
M31	33.240	86.840	8	5.3	8
M32	33.290	86.820	9	5.5	15
M33	27.660	86.000	16	5.4	8
M34	35.060	72.910	12	5.9	15
M35	32.390	78.500	9	6.2	13
M36	35.860	79.900	7	4.7	10
M37	33.130	92.840	7	5.6	5
M38	35.120	80.840	8	5.5	21
M39	35.830	79.920	9	5.6	17
M40	31.950	78.590	6	5.1	17
M41	32.570	78.490	8	5.5	16
M42	32.780	104.090	12	6.1	2
M43	32.590	104.240	5	6.0	1
M44	32.490	104.180	8	6.2	2
M46	38.190	90.970	8	5.8	6
M47	37.020	95.730	14	5.8	2
M48	32.650	88.390	11	5.7	11
M49	32.980	82.260	11	5.5	23
M50	35.470	82.000	6	5.0	19
M51	32.440	97.260	12	5.4	7
M52	29.930	80.270	16	5.7	12
M53	26.740	87.480	20	4.6	8
M54	30.550	88.650	6	6.3	9
M55	38.910	95.600	12	5.2	6
M56	33.000	88.550	11	5.1	12
M57	29.340	81.210	14	5.7	13
M58	29.630	81.090	18	6.1	16
M59	32.960	75.750	14	5.2	16
M60	32.900	75.800	13	5.2	17
M61	35.620	82.140	4	5.4	19
M62	27.400	88.800	44	6.1	9
M63	30.890	101.150	7	5.7	5
M64	34.510	91.420	9	5.3	12
M65	35.680	73.600	7	6.1	19
M66	31.680	82.280	9	6.0	15
M67	31.850	99.920	9	5.5	12
M68	35.560	87.200	8	5.2	26
M69	32.150	76.400	13	5.5	25
M70	31.220	86.820	9	5.9	15
M71	34.450	79.930	5	4.4	13
M72	31.050	78.000	13	5.6	23
M73	34.560	91.640	11	5.5	18
M74	37.740	101.520	7	6.1	8
Z05	31.230	93.560	8	5.5	2
Z31	40.050	75.170	5	5.6	17
Z37	38.120	91.130	15	5.7	18
Z38	41.400	89.660	20	5.8	12
Z39	34.340	91.790	8	6.4	27
Z40	30.040	99.130	8	6.3	19
Z41	30.050	99.430	8	6.1	17
Z42	30.070	99.490	9	6.1	14
Z43	30.130	99.550	8	5.9	15
Z44	31.610	102.520	12	6.3	9
N01	41.518	88.713	0	6.2	7
N02	41.768	88.380	0	4.6	1
N03	41.569	88.701	0	5.4	12
N04	41.514	88.739	0	6.2	17
N05	41.513	88.774	0	6.6	21
N06	41.716	88.336	0	5.1	11

RA Events taken from *Randall et al.* [1995]; M events taken from *Molnar and Lyon-Caen* [1989]; Z events taken from *Zhao and Xie* [1993]; N explosions taken from *Gupta* [1995].

Travel Time Selection Criteria

Travel times used in this study are from two sources. The first group was obtained from recordings using 11 broadband Streckeisen STS-2 sensors deployed for 1 year within the Tibetan Plateau (Figure 1) (Table 2) (see *Owens et al.*, [1993]). *Pn* arrival times were picked as the first motion on the high-frequency (0.5-4 Hz) vertical component traces at regional distances ($3° \leq \Delta \leq 16°$) from the portable network [*McNamara et al.*, 1995]. In addition, arrivals at 69 stations were obtained from the ISC catalogs to increase the ray coverage across the Tibetan Plateau (Figure 1) (Table 2). *Zhao and Xie* [1993] showed that ISC arrival times are generally accurate to at least 0.5 s. We did not examine waveforms; consequently, the chance for error was increased with these data. Many factors introduce systematic late travel time picks in the ISC data set [*Hearn et al.*, 1991; *Grand*, 1990]. For this reason, we apply strict data selection criteria and rely on the large number of observations to minimize error. We also have limited our data set to events that have published locations improved from the original Preliminary Determination of Epicenters (PDE) and ISC locations. ISC event locations are systematically deep [*Zhao and Helmberger*, 1991; *Randall et al.*, 1995; *Molnar and Lyon-Caen*, 1989] and can produce an overestimation of about 1.5% for *Pn* velocity within the plateau [*Zhao and Helmberger*, 1991; *Holt and Wallace*, 1990]. The systematic depth error is likely due to the anomalously thick crust beneath the plateau (60-70 km) [*McNamara et al.*, 1995; *Molnar*, 1988]. To avoid potential ISC location bias, we obtained improved depth estimates from four different sources (Figure 1 and Table 2). First, 79 ISC events with improved locations and depths were obtained from the teleseismic waveform modeling techniques of *Molnar and Lyon-Caen* [1989] and *Zhao and Helmberger* [1991]. An additional 40 events were relocated by modeling long-period regional waveforms recorded at the portable stations common to this study [*Randall et al.*, 1995]. Finally, six explosion sources located at the Chinese Lop Nor test site were included since their locations were improved using a variety of techniques by *Gupta* [1995]. Source and receiver locations

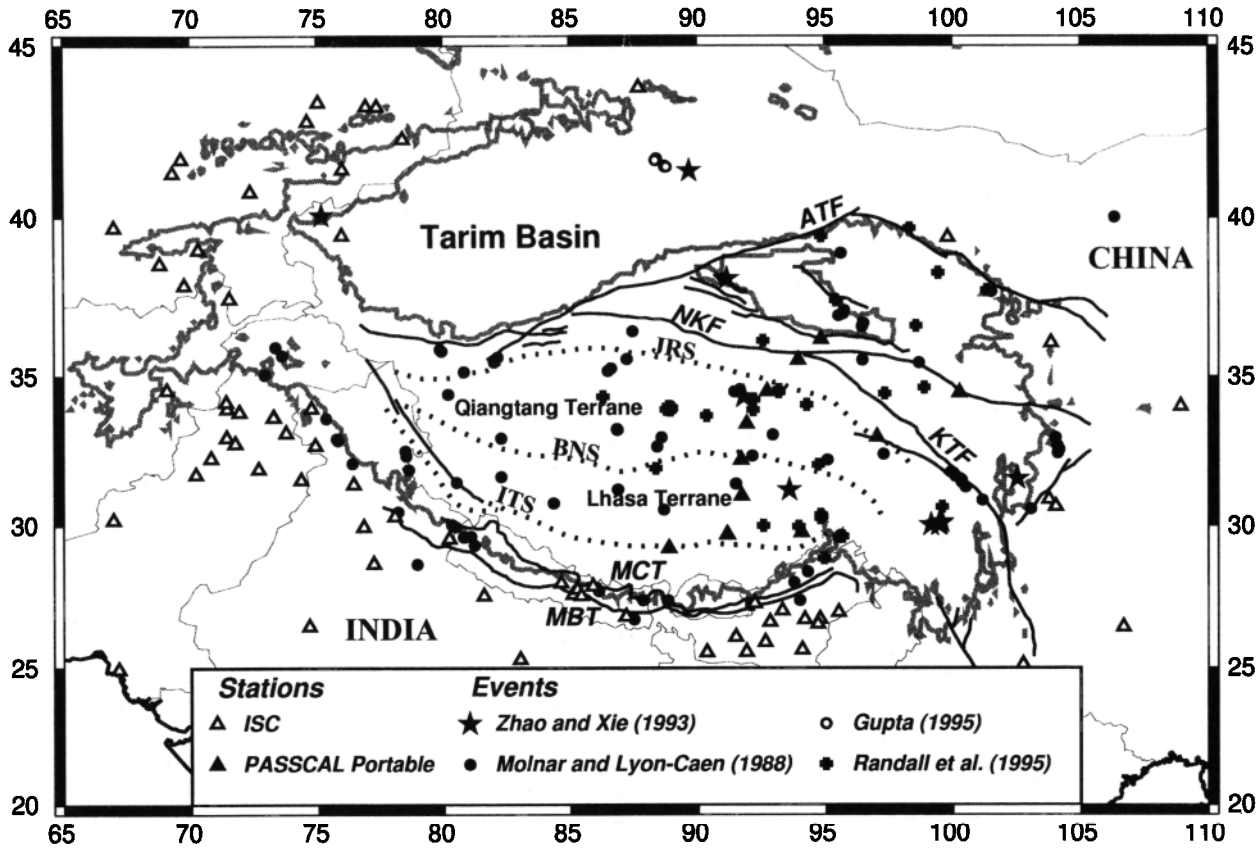

Figure 1. Map of the Tibetan Plateau showing recording stations (diamonds) and the distribution of regional events used in the backprojection tomography (see legend). Regional structural trends are taken from *Dewey et al.* [1988]. Solid lines show major faults (ATF, Altyn Tagh Fault; NKF, North Kunlun Fault; KTF, Kang Ting Fault; MCT, Main Central Thrust; MBF, Main Boundary Thrust), and dashed lines indicate suture zones that bound tectonic terranes of the plateau (JRS, Jinsa River Suture; BNS, Banggong Nujiang Suture; ITS Indus-Tsangpo Suture). The 3000-m contour is shown as a thick gray line.

were limited in longitude from 65° to 110°E and latitude from 20° to 45°N and events less than magnitude 4.0 were excluded.

The selected distance range is based on results from *McNamara et al.* [1995], who showed that the the *Pg*-*Pn* cross over distance within the Tibetan Plateau is approximately 300 km and that the distance at which deeper turning *P* waves arrive first occurs at about 1800 km. Owing to scatter in the travel time data, exact crossover distances are difficult to precisely estimate. To isolate *Pn* from slower *Pg* and faster *P* waves, we narrowed the acceptable range to 333-1600 km (Figure 2a). Between these distances, travel times are nearly linear, indicating a consistent average *Pn* velocity and negligible effects of a mantle lid velocity gradient (Figure 2b). As is readily observable in Figure 2a, large residuals are common within the ISC data set due either to systematic misidentification of phases and/or measurement errors. To limit travel time residuals not related to structural variations, we used only first arrivals in the ISC catalogs. We also calculated individual event/station apparent velocities, with an average crustal correction of 14.34 s, and required velocity perturbations to be within 10% of the average fit (8.3 km/s) to the entire data set (Figure 2a). By applying these criteria, we reduced the occurrence of ISC-picking-error-induced travel time residuals. Any remaining travel time residuals are likely due to lateral *Pn* velocity variations.

By applying these strict data selection criteria, we collected 1510 high-quality *Pn* travel times, nearly 400 of which were picked in this study. These 400 paths propagated completely within the Tibetan Plateau. Figure 3 shows the distribution of ray paths across the region. Ray path coverage is best in the eastern portion of the plateau due to the distribution of the portable stations and is weakest in the north central plateau and the Tarim basin due to the limited distribution of events and ISC stations. Our data set contains over 4 times the number of ray paths used in previous *Pn* tomographic studies within the region [*Zhao and Xie,* 1993].

Inverting Travel Times for Slowness

Method. First, we assume that *Pn* is a head wave that travels directly beneath the Moho (Figure 4), and therefore lateral velocity variations are confined to a single layer of the upper most mantle. Then the *Pn* travel time can be divided into three parts: a mantle leg, one crustal leg beneath the recording station, and another crustal leg beneath the source (Figure 4); its travel time can be expressed by the time term equation

$$t = a + b + Ds \tag{1}$$

where t is the total travel time, D is the source-to-receiver distance, s is the mantle slowness, a is the event delay correction, and b is the station delay correction [*Hearn and Clayton,* 1986; *Hearn et al.,* 1991]. The static delays, a and b, are expressed by

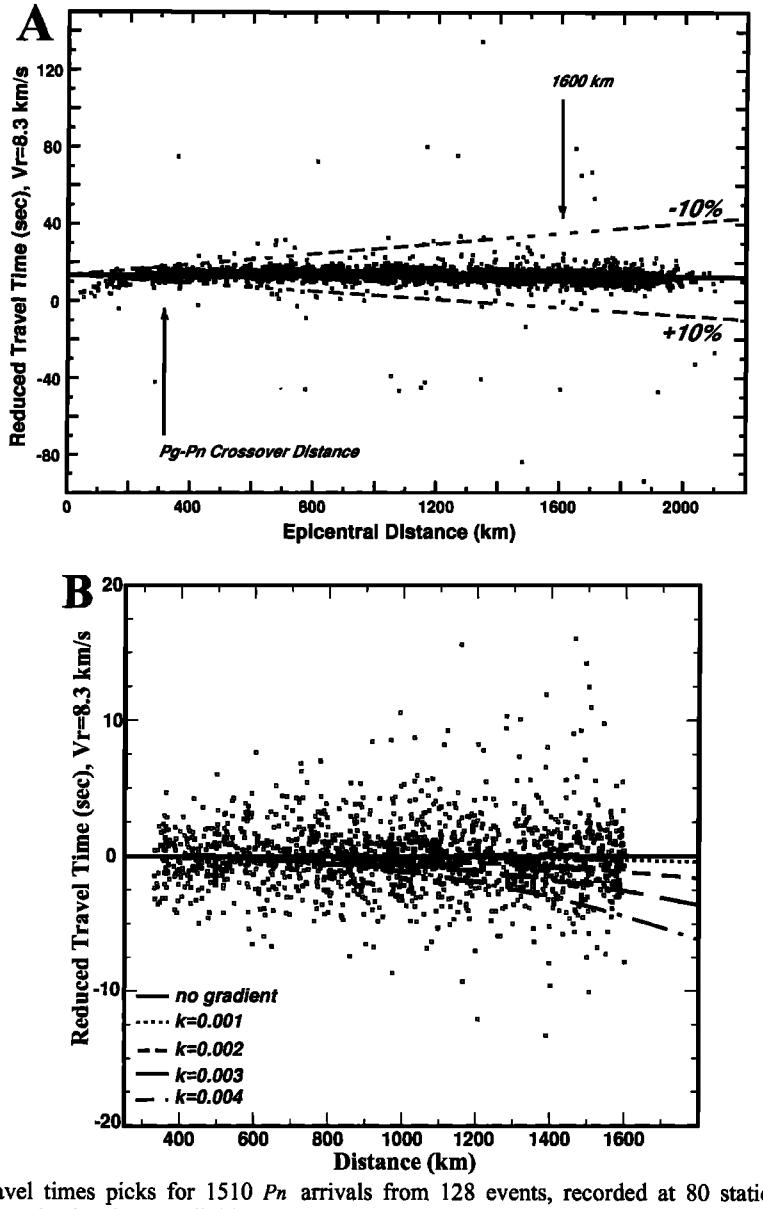

Figure 2. (a) Travel times picks for 1510 *Pn* arrivals from 128 events, recorded at 80 stations, between distances of 333 km and 1600 km. Individual apparent velocities were constrained to be less than ±10% of the average velocity for the entire data set (8.3 km/s). Travel times that passed our data selection criteria are shown as solid squares; others are shown in as open squares. (b) *Pn* travel times are shown with a reducing velocity of 8.3 km/s with travel time curves expected for a range of upper mantle velocity gradients. RMS residuals are smallest for the linear (no gradient) fit.

$$delay = \int (s_c^2 - s^2)^{0.5} dz \qquad (2)$$

where s_c is the crustal slowness profile as a function of depth. For estimating the velocity variations across the Tibetan Plateau, we have gridded the upper mantle into 900 1° cells. The slowness in each cell can be estimated using a modified time term equation. An individual ray travel time equation becomes the sum of the path lengths traveled within each cell multiplied by the cell slowness plus the crustal static delays:

$$t = a + b + \sum d_i s_i \qquad (3)$$

where d_i is the distance the ray travels in cell i and s_i is the slowness in cell i.

We follow the method outlined by *Hearn* [1984]. First, residuals are calculated from the mean fit to the raw travel time data (8.3 km/s). Next, source static delays are estimated by the mean residual for each event. Source delays are removed, and new residuals are calculated. Station static delays are then estimated by the mean residual for each station. Station delays are removed, and new residuals are calculated. Finally, using (3), slownesses are estimated as the weighted mean of the apparent slownesses of all rays traversing each cell. The factor used to weight individual slownesses is the product of the total ray path length and the portion of the path within a particular cell. Between iterations, we smooth the model to eliminate extreme slowness estimates due to poorly sampled cells by averaging the value of each cell with the surrounding eight cells. Using this new slowness model, new residuals are calculated and the process is repeated. Iteration continued until the RMS residual change was less than 1% between iterations (usually <10 iterations).

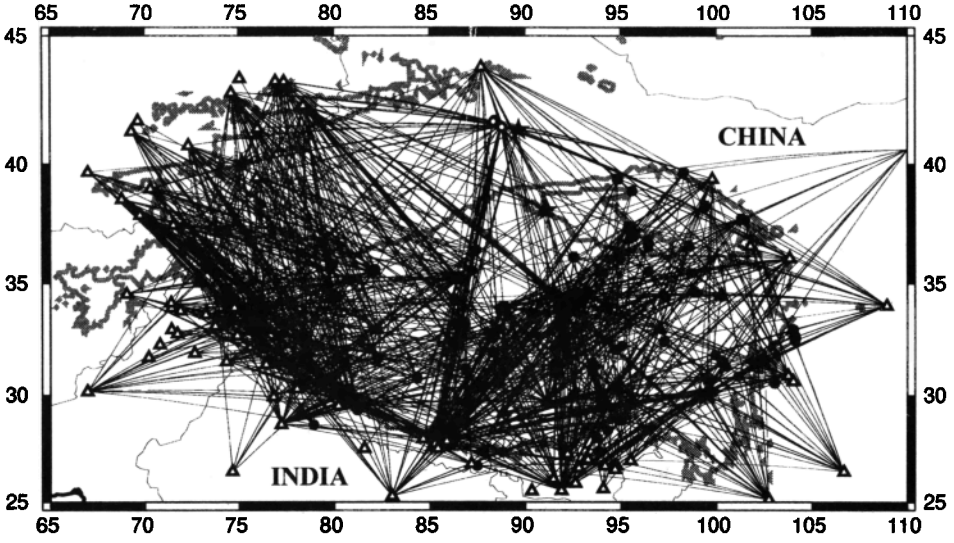

Figure 3. Ray path distribution of *Pn* travel times used in the backprojection procedure. Triangles are stations, and circles are earthquakes. The grey line marks the 3000-m contour.

Data resolution. A first-order measure of data set resolution can be obtained by inspecting the ray path distribution within a particular region (Figure 3). Ray path density is important, but azimuthal sampling is more significant. To qualitatively estimate the resolution of our data, synthetic travel times were computed for alternating-velocity "checkerboard" test models, and these travel times were inverted. Synthetic travel times were computed using the distribution of rays obtained from the actual data set, and the travel times were inverted in the same manner as the observed data set. By comparing the inversion results to the input test models, the resolution of the data set can be assessed across the sampled region. We tested several models for our resolution analysis. Each was a "checkerboard" model with alternating perturbations about an average velocity. Perturbations differed in magnitude and areal extent. Using a range of models, we estimated minimum anomaly size and perturbation resolvable, with our data.

In Figure 5, we present the inversion results, after 10 iterations, from two different test models. Each has an alternating velocity pattern that varies by ±3% about an average of 8.3 km/s. In Figure 5a, we show the inversion results for a model with 5°, alternating *Pn* velocity, blocks; in Figure 5b, the target model had smaller 3° blocks. Our ray path coverage is sufficient to detect the 5° velocity pattern across the entire plateau and most of the Tarim Basin to the north. Perturbations tend to be underestimated toward the edges of the grid, but anomalies are properly located across most of the region. The ability to resolve anomalies as small as 3° breaks down across most of the plateau, except within the area of our portable array (Figure 5b).

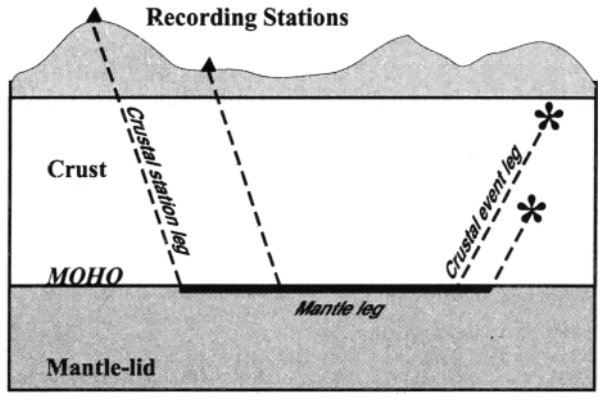

Figure 4. Schematic diagram of the three-leg *Pn* ray path when modeled as a head wave. The tomographic method solves for delays associated with the event and station crustal legs as well as lateral velocity variations along the mantle leg of the ray path.

The underestimation of velocity perturbations at the edges of the grid is likely an effect of limited azimuth coverage near the edges. Most ISC stations are located toward the boundaries of the sampled region which causes poor distribution of ray paths beneath each station (Figure 3). Without full azimuth distribution, the trade-off between the crustal delay and the mantle velocity anomaly at each station cannot be resolved. For this reason, we will not interpret the crustal station delays for the ISC stations. By comparing the ray distribution (Figure 3) to the inversion results of Figure 5a, we observe that azimuthal distribution is the most significant factor controlling resolution of a particular region. As expected, *Pn* velocity estimates will be most reliable within the center of the study area and least reliable toward the edges.

Anisotropy effects. *McNamara et al.* [1994] analyzed *SKS* shear wave splitting and reported strong variable fast azimuths and splitting values between each station indicating a complex pattern of anisotropy within the upper mantle across the Tibetan Plateau. Two of the largest values of splitting ever observed were reported at stations common to this experiment (BUDO, ERDO) indicating that anisotropy must certainly affect *Pn* travel times used here. We have analyzed individual paths and have not been able to find a pattern between apparent *Pn* velocity and azimuth of propagation, suggesting that the complicated pattern of anisotropy is difficult to resolve. Techniques exist to solve for *Pn* velocity anisotropy using tomographic inversion techniques [*Hearn,* 1996, 1984; *Hirahara and Hasemi,* 1994]. *Hearn* [1996] showed that it is possible to solve for both lateral velocity and anisotropy variations simultaneously with a very large data set (30,000 paths) in the

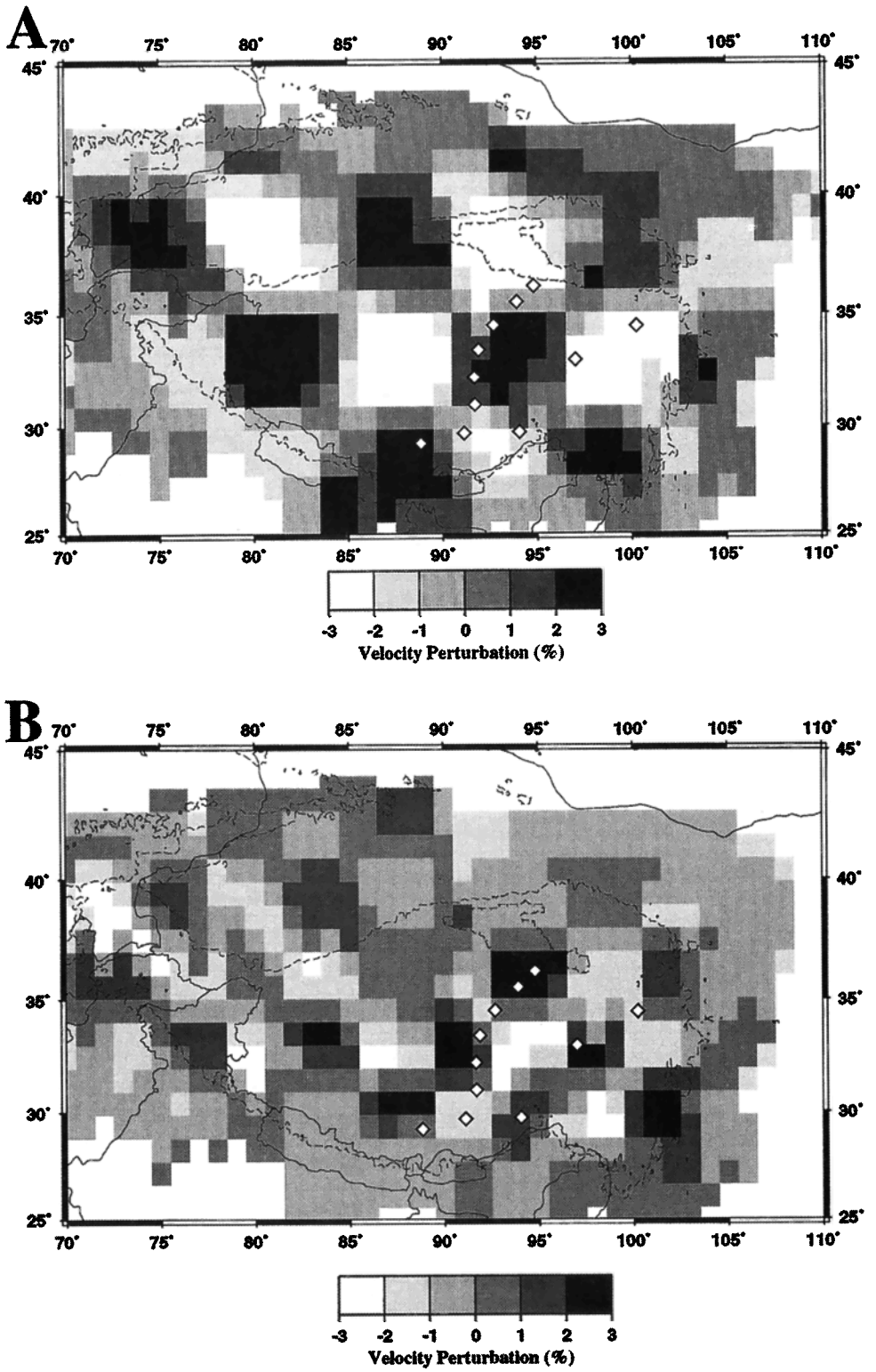

Figure 5. Inversion results from input velocity models used to investigate data set resolution. Input model velocity anomalies alternate in a checkerboard pattern. Shown are (a) 5° x 5° alternating 3% velocity perturbation about an average of 8.3 km/s, and (b) 3° x 3° alternating 3% velocity perturbation about an average of 8.3 km/s. PASSCAL portable array stations are shown as diamonds for reference.

western United States. However, he found that by including the effects of anisotropy the major velocity anomaly pattern did not change though the amplitude of the variations was reduced. This result suggests that the velocity variations that we observe within the Tibetan Plateau will remain; however, by including the effects of anisotropy the 3-4% velocity difference might be slightly reduced.

Mantle lid velocity gradient effects. Finally, *Pn* ray paths, in the presence of a significant mantle lid velocity gradient, will deviate from the simple refraction model assumed here. In the

presence of a velocity gradient, *Pn* observed at different distances will sample the mantle at different depths significantly biasing travel times. Previous studies of regional phase velocity within the Tibetan Plateau have reported a range of mantle lid velocity gradients (0.0025-0.0031 $kms^{-1}km^{-1}$) [*Holt and Wallace,* 1990; *Zhao and Xie,* 1993]. Although these gradients are weak relative to worldwide sub continental mantle lid gradients, some error in the travel time data, due to ray path distortion, could occur. Owing to the linear trend of our 1510 *Pn* travel times (Figure 2b) we find little evidence for a significant velocity gradient beneath the Tibetan Plateau. In a related study we directly investigated the potential effect on our inversion results by correcting individual *Pn* ray paths for several assumed mantle lid compressional wave velocity gradients [see *McNamara,* 1995]. *McNamara* [1995] modeled *Pn* as a diving wave rather than a head wave. A backprojection method similar to the head wave procedure was used, except that a correction to invert for the P wave velocity directly beneath the Moho was applied by assuming the velocity-depth function:

$$V(z)=V_0+kz \tag{4}$$

where $V(z)$ is the mantle velocity as a function of depth, V_0 is the velocity at the top of the gradient, which in our case is at the base of the crust, directly beneath the Moho, k is a measure of the gradient with units $kms^{-1}km^{-1}$, and z is the depth of penetration of the circular diving ray path. Inversions were performed assuming a range of different P wave velocity gradients within the upper mantle. The smallest represents a gradient due only to the curvature of the Earth (k=0.001 s^{-1}), and the largest is a stronger gradient in the higher range of values previously reported for the Tibetan Plateau (k=0.004 s^{-1}). In general, we found that models generated by assumption of a diving wave produced unrealistic velocity variations throughout the region, and residuals were best reduced for weaker gradient assumptions but none were reduced as well as in the head wave case. Figure 2b demonstrates the observation that *Pn* is best modeled as a head wave within the region, showing 1510 travel times reduced by the average velocity of 8.3 km/s along with travel time curves expected for a range of upper mantle velocity gradients. Travel time in the presence of a velocity gradient is expressed by

$$t=\frac{2}{k}\sinh^{-1}\frac{kD}{2v_0} \tag{5}$$

and is shown in Figure 2b for a k=0.001 to 0.004. The RMS residuals for the stronger gradients (k=0.002-0.004) are significantly larger than for the linear (no gradient) fit and the weakest gradient (k=0.001). This suggests that a weak to negligible gradient may exist and that modeling *Pn* as a head wave is a better representation of the ray path for our regional data set. We therefore use our simple head wave inversion results and discuss only first-order features in the image.

Inversion Results

Velocity variations beneath the Tibetan Plateau. Using the 1510 ray paths selected with the previously discussed criteria, we next inverted the observed *Pn* arrival times in the same manner as our synthetic tests. Velocity perturbations from the average are quite small across the plateau. All are less than 4%, and most are below 2-3%. Individual cell velocity was determined by adding the cell perturbation, determined from the inversion procedure to average velocity computed for the entire data set (8.3 km/s) and then multiplying by a factor of (R_E-h/R_E) to correct for the sphericity of the Earth [*Zhao and Xie,* 1993]. R_E is the radius of the Earth and was assumed to be 6371 km. For the depth to the refractor h we assumed a crustal thickness of 65 km [*McNamara et al.,* 1995], which will slightly underestimate velocities for areas with thinner crust but will allow more accurate velocities within the plateau, where our data resolution is best.

The resulting *Pn* velocity image is shown in Plate 1. We observe variations that range from about 8.0 to 8.3 km/s after all corrections are applied (Plate 1). In Figure 6 we show the residual improvement from the first to the last iteration. The average travel time residual is decreased from 1.26 s to 0.55 s after eight iterations. Note the residual reduction by the growth of the peak centered at a residual of 0 s from the first to the last iteration (Figure 6). Residuals for the first iteration are relative to the data set average of 8.3 km/s. Residuals for the last iteration are relative to the *Pn* velocity model after eight iterations. Generally, few iterations are required to construct the main features of the image. Stopping the inversion early suppresses poorly resolved features of the image by eliminating extreme velocity anomalies in poorly sampled cells.

Comparison with previous geophysical studies. The overall model pattern can be characterized by a relatively low-velocity (8.0-8.1 km/s) region throughout much of the northern Tibetan Plateau and a higher-velocity zone (8.1-8.3 km/s) in the southern portion of the plateau (Plate 1). The north to south velocity variations that we observe are in general agreement with a previous *Pn* backprojection study within the plateau. However, our results diverge from the results obtained by *Zhao and Xie* [1993] in two ways. First, our average *Pn* velocity is higher than reported by *Zhao and Xie* [1993] (7.93 km/s). This is likely due to the inclusion of the effect of a mantle lid velocity gradient by *Zhao and Xie* [1993]. As previously discussed, gradient effects are negligible in our data set. Second, *Zhao and Xie* [1993] report a *Pn* low-velocity zone, limited to the north central portion of the plateau, that is coincident with a region of inefficient *Sn* propagation reported by *Ni and Barazangi* [1983]. We show relatively low *Pn* velocities throughout a larger portion of the northern plateau (Plate 1). The difference between the low *Pn* velocity region reported by *Zhao and Xie* [1993] and our results is likely due to their limited ray density and distribution that did not enable as complete a sampling of the entire plateau. With a more complete data set, and using stations within the plateau, common to this study, *McNamara et al.* [1995] have shown that the region of inefficient *Sn* propagation is significantly larger than originally mapped by *Ni and Barazangi* [1983] (Plate 1). The newly defined region of inefficient *Sn* propagation includes a larger portion of the northern plateau and closely coincides with the low *Pn* velocity region determined in this study.

Correlation with regional tectonics. For regions surrounding the Tibetan Plateau, including the Hindu Kush and Pamirs to the west, the Himalaya and Karakoram along the southern boundaries, the Tarim Basin to the northwest and the Nan Shan Mountains to the northeast, *Pn* velocities range from (>8.1-8.3 km/s). Velocity variations across the entire region correspond well with regional geologic trends. For example, higher velocities observed correspond with relatively stable, undeformed areas (Tarim Basin), while the lowest velocity corresponds to a

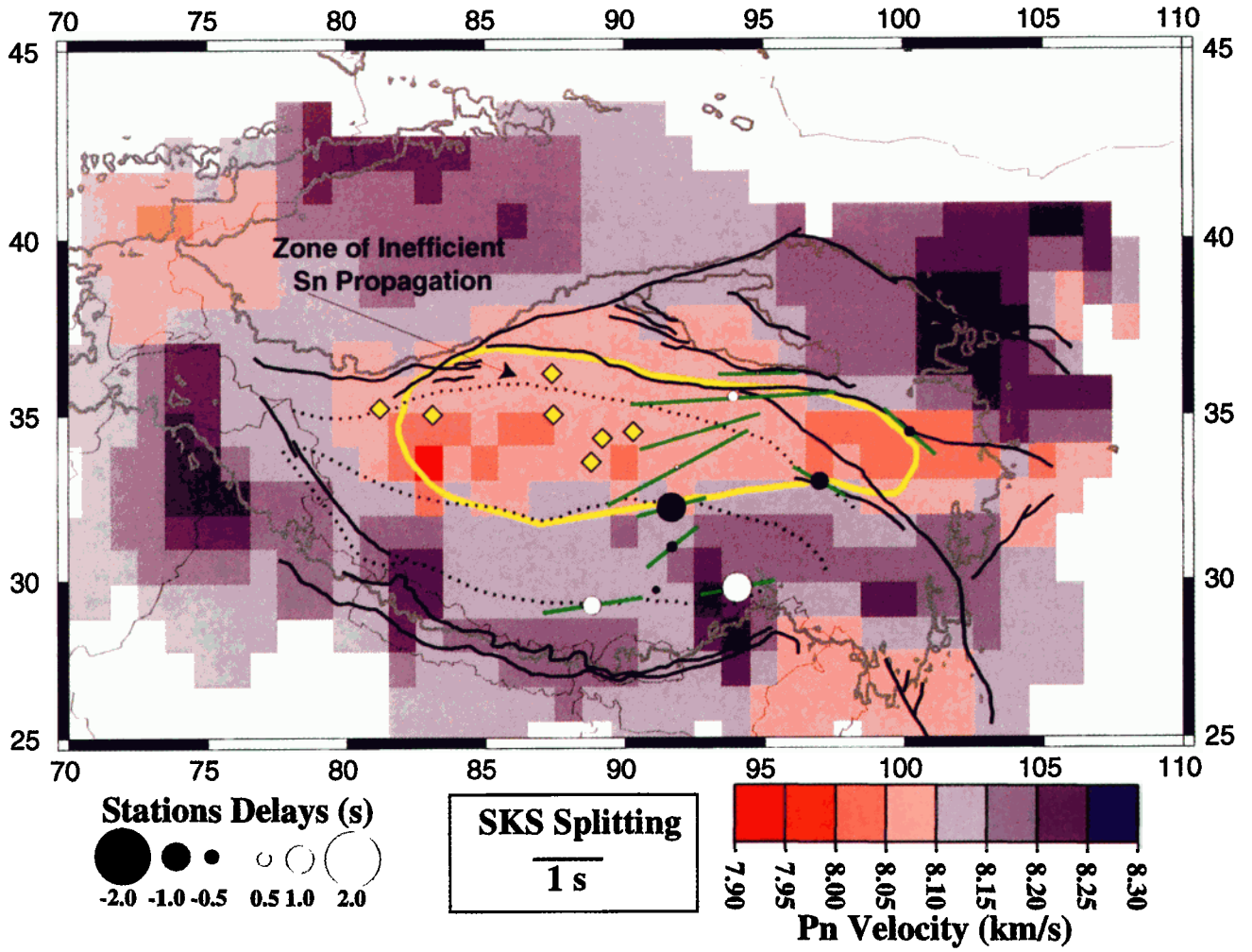

Plate 1. Two-dimensional velocity image for the uppermost mantle beneath the Tibetan Plateau when *Pn* is modeled as a head wave. Crustal delays are shown for the 11 portable stations deployed in the plateau. Positive delays reflect slow or thick crust, while negative delays indicate fast or thin crust. The thick gray line represents the 3000-m contour and regional structural trends are the same as in Figure 1. Also shown are results from previous studies in the region. Yellow diamonds indicate volcanic sampling locations [*Turner et al.*, 1993; *Arnaud et al.*, 1992]. A large zone of inefficient *Sn* propagation is shown within the region in yellow [*McNamara et al.*, 1995] and shear wave splitting measurements determined at the same portable stations are displayed as green lines [*McNamara et al.*, 1994].

region of young volcanism in the northern plateau [*Molnar, 1993; Arnaud et al.*, 1992; *Turner et al.*, 1993].

We, and others, have previously noted the possible correlation of the northern and southern extents of the zone of inefficient *Sn* propagation with the Banggong Suture and North Kunlun Fault, respectively [*Ni and Barazangi*, 1983; *McNamara et al.*, 1995]. Our *Pn* images support this interpretation in the south within the about +/100 km resolution that the method allows but is less obviously in agreement along the northern boundary. However, if we accept the idea that India has underthrust Asia to about the latitude of the Banggong Suture [*Beghoul et al.*, 1993; *Jin et al.*, 1996], then it is not clear that the correlation of the change in upper mantle structure with this suture is more than a coincidence since, at current convergence rates, India could not have progressed farther north since the onset of the collision.

In the north, our *Pn* image suggests that the low velocities extend some 200 km north of the Kunlun fault and their northern boundary may be more closely associated with the Altyn Tagh fault. *Ni and Barazangi's* [1983] suggestion of the association of the northern limit of the zone of inefficient *Sn* propagation was not strongly constrained by our more recent work [*McNamara et al.*, 1995], although consistent with their assertion, was also unable to significantly improve the resolution of this northern limit. Nonetheless, it is our belief that neither *Sn* study would be consistent with interpretations that extend the northern limit as far north as our *Pn* image suggests, and we suspect that the tomography is not able to resolve the northern boundary with greater accuracy than the *Sn* analysis. In fact, shear wave anisotropy analysis [*McNamara et al.*, 1994] and P wave teleseismic tomography [*Wittlinger et al.*, 1996] and differential attenuation of body waves (D. Guo and T. J. Owens, Differential attenuation of teleseismic *P* and *S* waves in the lithosphere beneath the Tibetan Plateau, submitted to Geophysical Research Letters, 1996) support the idea that the Kunlun front is a major lithospheric boundary.

Plate 1 also shows the resultant station delays for the 11 portable stations within the Tibetan Plateau. We present only

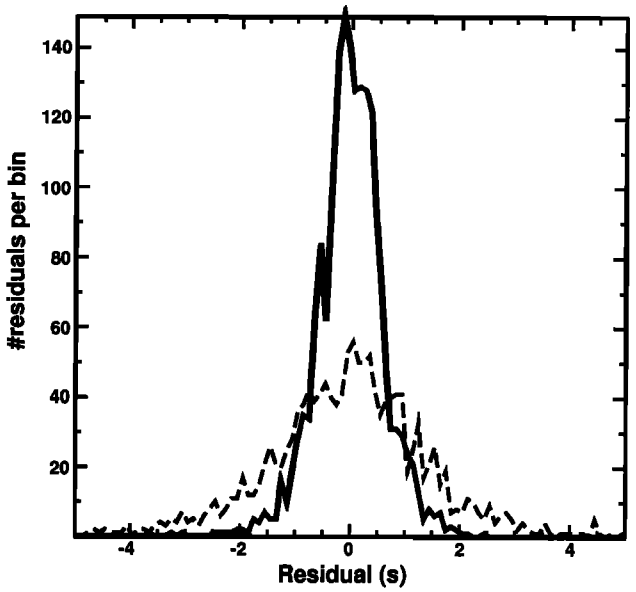

Figure 6. The dashed line shows residuals after one iteration. The solid line shows residuals after convergence (eight iterations). The average residual was decreased from 1.27 s to 0.55 s after eight iterations.

these 11 since delays from other stations are not interpretable due to the limited azimuthal distribution (Figure 3). Crustal delays are computed relative to a crustal thickness of 65 km and an average crustal velocity of 6.4 km/s [*McNamara et al.*, 1995]. Negative delays indicate thin or fast crust, and positive delays represent the effect of thick or slow crust. For northern stations (TUNL, BUDO, ERDO, WNDO) delays are less than 0.5 s, suggesting little variation from the initial crustal model. With the exception of XIGA and GANZ, stations to the south and east have small negative delays. Ray path coverage to southern most stations (XIGA, GANZ) is biased toward the north (Figure 3). Without good azimuthal distribution, station delays cannot be interpreted. From the intercept times determined using regionalized *Pn* ray paths, *McNamara et al.* [1995] demonstrated that the crust is at least 10 km thinner in the northern plateau relative to the south. The observed delays at the remaining stations do not follow a trend expected for a thin crust in the north relative to the south. For this reason, we suspect that station delays also reflect crustal velocity variations as well as thickness. Studies using Rayleigh wave propagation across the plateau and receiver functions have reported evidence for low crustal velocities in the northern plateau [*Brandon and Romanowicz*, 1986; *Zhu et al.*, 1995].

Discussion

Our results indicate significant variations in the compressional wave velocities in the uppermost mantle beneath the Tibetan Plateau. The implied variation of approximately 3% is indicative of significant variations in upper mantle temperature, pressure, composition, or a combination of these factors. In this section, we discuss some of the implications of the observed variations on the structure of the uppermost mantle.

Pressure effects. We first discuss the effects of pressure to make an estimate of the average velocity difference between the northern and southern plateau and to compare those values with upper mantle velocities beneath other continental regions. The *Pn* velocities that we have observed (7.95-8.3 km/s) span the average worldwide sub continental *Pn* velocity of about 8.1 km/s [*Mooney and Braile*, 1989] with a tendency to be slightly fast. However, the atypical thickness of the crust [*Molnar*, 1988; *McNamara et al.*, 1995] of the plateau requires a correction for the effects of both the increased pressure and increased earth curvature at greater depths before comparison with global averages. The average crustal thickness difference between the northern and southern plateau is estimated to be between 10 and 17 km based on the observation that the intercept time of the *Pn* travel time curve for paths confined to the southern plateau is 3.1s greater than the intercept time determined for paths confined to the northern plateau [*McNamara et al.*, 1995]. This effect alone would account for only 0.03 to 0.05 km/s of the observed *Pn* velocity differences using the velocity-pressure relation of *Anderson et al.* [1968]. If we use average crustal thicknesses of 70 km in the southern plateau, and 57 km in the northern plateau, and standard formulas for the effects of curvature [*Chapman and Orcutt*, 1985] and pressure [*Anderson et al.*, 1968], we get equivalent average *Pn* velocities at the base of a 40-km crust of 7.91 km/s in the north and 8.12 km/s in the south. These suggest that *Pn* velocities beneath the northern plateau are similar to velocities generally observed in tectonically active regions [*Hearn et al.*, 1991; *Beghoul et al.*, 1993], while in the south, the values are comparable to global averages.

The most significant result from our *Pn* velocity tomographic inversion is the pronounced lateral variation across the Tibetan Plateau (Plate 1). This is the latest, and highest-resolution, evidence to date, in a body of evidence that indicates that a large portion of the northern Tibetan Plateau is anomalous relative to the southern plateau and surrounding regions. In general, the geological and geophysical evidence suggests the existence of higher temperatures in the northern plateau relative to the southern plateau. The low *Pn* velocities underlie a region where late Cenozoic lava flows and active volcanos have been observed in the northern Tibetan Plateau [*Arnaud et al.*, 1992; *Deng*, 1978; *Turner et al.*, 1993]. Previous studies in the northern plateau also have reported evidence for slower shear velocities from observations of large teleseismic *S-P* travel time residuals [*Molnar and Chen*, 1984; *Molnar*, 1988], from modeling *SS* phases whose bounce points are beneath the Tibetan Plateau [*Woodward and Molnar*, 1995; *Lyon-Caen*, 1986], and from modeling Rayleigh wave group velocities [*Brandon and Romanowicz*, 1986]. Other studies have also identified low *Pn* velocities [*Zhao and Xie*, 1993; *Holt and Wallace*, 1990], and inefficient *Sn* propagation [*McNamara et al.*, 1995; *Ni and Barazangi*, 1983] (Plate 1). The most recent geometry of the region of inefficient high-frequency *Sn* propagation [*McNamara et al.*, 1995] and anomalously large shear wave splitting values [*McNamara et al.*, 1994] are shown with our *Pn* tomography image on Plate 1. In contrast, the high *Pn* velocities reported here and efficient *Sn* propagation [*Ni and Barazangi*, 1983; *McNamara et al.*, 1995] in the southern plateau can be combined with the observation of several intermediate depth, sub crustal earthquakes to suggest that the southern plateau mantle lid is cold, with temperatures in the range required to support brittle failure (600°C-800°C) [*Molnar and Chen*, 1983; *Zhu and Helmberger*, 1996]. Such comparisons have lead to suggestions that the northern Tibetan Plateau mantle lid is as much as 600°C warmer than the south and that this large lateral thermal gradient can only be explained by upwelling asthenosphere [*Molnar*, 1993; *Beghoul et al.*, 1993].

Thermal effects. *Pn* is generally most sensitive to thermal variations in the upper 30 to 40 km of the mantle [*Hearn et al.*, 1991], although the studies cited above would suggest that these physical property variations may extend to greater depths (>250 km). We can compute rough temperature estimates within the uppermost mantle by assuming temperature derivatives determined in laboratory experiments and then applying existing geologic information. Qualitative estimates of lateral temperature variation, based on seismicity and geologic observations [*Molnar*, 1988, 1993] are consistent with common temperature/velocity relations [*Soga et al.*, 1966; *Isaak*, 1992] and range from about 600 to 700°C across the plateau. The mantle lid beneath southern plateau is cold enough to support sub crustal earthquakes (600-800°C) so using these relations the mantle lid beneath the northern plateau could be at temperatures as high as those expected at the top of the asthenosphere (~1350°C). However, more recent experiments that take into account the realistic effects of anelastic behavior suggest that the temperature variations required may be roughly a factor of 2 smaller than previously reported [*Karato*, 1993]. The basis of these studies is that high-frequency laboratory measurements do not directly extrapolate to the behavior of longer-period seismic waves without adjusting the temperature derivatives for energy loss due to anelastic behavior. This is accomplished by including the effects frequency dependent propagation quality (where Q is the quality factor; the inverse of attenuation).

There is little information available regarding Q_P within the upper mantle beneath the Tibetan Plateau. However, D. Guo and T. J. Owens (submitted manuscript, 1996) have used differential attenuation of teleseismic phases to demonstrate the attenuation is significantly higher in the northern plateau relative to the southern plateau. Since *Pn* velocity is not sensitive to Q_P, we can assume a reasonable average for the region based on the laboratory results and seismic observations of Q in other tectonically active regions where the upper mantle may be similar to the Tibetan Plateau. High temperature and pressure laboratory experiments (1230°C, 0.73 GPa) estimate Q_P at the depth of *Pn* penetration to range from about 100 to 300 [*Sato et al.*, 1989]. Q_P extrapolated from measurements of Q_S from surface waves traversing the Basin and Range of North America are low (<100) [*Patton and Taylor*, 1984] and may be comparable to Q_P beneath the Tibetan Plateau. Assuming a range of possible Q_P=100-300 and applying the temperature derivatives that account for anelastic effects of *Karato* [1993], a 3% *Pn* velocity variation can be explained by a thermal variation of about 240-340°C. Q_P at 1000 yields a temperature difference increase to only 370°C, so the exact choice of Q_P is not critical given the range of uncertainty in the initial upper mantle temperature estimate in the southern plateau. This analysis suggests that for a range of possible Q_P from 100 to 1000 and assuming temperatures of 600°C to 800°C in the uppermost mantle of the southern plateau, the upper mantle temperatures in the lid of the northern plateau could be as low as 840°C to 1170°C. Based on the Basin and Range Q measurements of [*Patton and Taylor*, 1984] we believe that the the lower temperatures are more likely to exist within the upper mantle beneath the Tibetan Plateau. In any case, it is significant that our new estimates are clearly less than 1200°C.

Composition effects. A distinction between temperature and compositional effects is difficult to make since elevated temperatures could cause compositional differences, through partial melt, that affect *Pn* velocity. It is likely that such compositional variation is manifested by partial melt of the mantle-lid beneath the northern plateau since inefficient propagation of *Sn* is often interpreted as an indication of partial melt in the upper mantle (A. J. Rodgers et al., submitted manuscript 1996); [*McNamara et al.*, 1995; *Gajewski et al.*, 1990]. The coincidence of low *Pn*, inefficient *Sn* propagation, and young volcanic rocks at the surface clearly indicates the existence of elevated temperatures and partial melt of the upper mantle beneath the northern plateau. (Plate 1)

The bimodal lavas and volcanos observed in the northern portion of the Tibetan Plateau have been active since about 13 Ma [*Arnaud et al.*, 1992; *Turner et al.*, 1993]. The widespread yet low volume nature of the lava flows suggest sporadic melting of lithosphere rather than a single asthenospheric plume source. The basaltic lavas are also rich in potassium (K) and other incompatible elements indicating a sub continental lithospheric mantle source rather a deeper, upwelling asthenospheric source. The K-rich basaltic lavas lead *Turner et al.* [1993] to suggest that the lower lithosphere was depressed downward during lithospheric thickening prior to 13 Ma. At depth, the K-rich layer is heated and passes through its wet solidus (700-900°C) to produce the potassium-basaltic melt. In contrast, *Arnaud et al.* [1992] invoke a southward subduction of Asian mantle lithosphere beneath the northern plateau and subsequent melt to supply the K-rich basaltic magma or else melting of the lower lithosphere due to small-scale convection of hot upwelling asthenospheric material. In either case, the volcanic compositions suggest the heating and melting of a sub continental lithospheric mantle lid rather than asthenosphere.

Our *Pn* results, constrained by laboratory estimates of anelastic behavior, suggest a temperature range of 840-1170°C, which is sufficient to induce partial melting of wet lithospheric mantle but low enough that the upper mantle is unlikely to be asthenosphere. Combined with the compositional constraints, this observation leads us to conclude that the uppermost mantle beneath the northern Tibetan Plateau is most likely partially melted mantle lithosphere. This partially melted mantle lithosphere gives rise to the observed low *Pn* velocities and inefficient *Sn* propagation in the northern plateau. This region of hot lithosphere may also lead to the observed enhanced shear wave anisotropy in the northern plateau through the activation of glide systems in olivine that takes place at temperatures of 800°C to 1200°C [*Durham and Goetze*, 1977] and, more speculatively, through the melting and removal of weakly anisotropic minerals such as pyroxene and amphibole. Although the depth distribution of upper mantle anisotropy is a complex function of temperature, pressure, mineral grain size, and strain [*Karato and Wu*, 1993, *Zhang and Karato*, 1995], one could also argue that significantly higher temperatures at the top of the mantle increases the likelihood that mode of olivine deformation in the mantle will transition to diffusion creep at a depth that leads to an anisotropic layer too thin to produce the observed (> 2 s) shear wave split times present in the northern plateau.

Implications for tectonic models of the Tibetan Plateau. The *Pn* tomographic image from this study and the related inference of cold lithosphere in the southern plateau and hot, partially melted, lithosphere in the northern plateau have some important implications for models of plateau evolution. We find relatively high *Pn* velocities in the southern plateau, south of about 32°N. It has been previously proposed [e.g. *Beghoul et al.*, 1993] that the higher upper mantle velocities in the southern plateau are evidence that India has underthrust beneath Asia to approximately 32°N. This assertion is supported by

more recent studies of gravity data in the plateau [*Jin et al.*, 1994, 1996] We suggest that this is the simplest interpretation of our observations of the high upper mantle velocities in the southern plateau.

This hypothesis would imply that a substantial portion of the Asian mantle lid has been removed from beneath the southern plateau. It is the fate of this material and the origin of the anomalous heat in the northern plateau that are the most uncertain aspects of tectonic models of the plateau. Delamination [*Houseman et al.*, 1981], convective instability [*Molnar*, 1993], and in situ shear heating [*McNamara et al.*, 1994] have all been proposed as means of resolving the problem of producing high temperatures as a result of lithospheric thickening. Our results and the geochemical studies [*Turner et al.*, 1993] provide the important constraint that at least the upper 30-40 km of the mantle is of lithospheric origin, not asthenospheric origin. This would seem to preclude models in which the entire mantle lithosphere has been removed and replaced with asthenospheric material. It does not preclude models that invoke convective upwelling of asthenospheric material as long as that material has not eroded the entire mantle lithosphere beneath the northern plateau. Recent teleseismic P wave tomographic results [*Wittlinger et al.*, 1996] suggest that an upwelling of low-velocity material extents only to within 150-200 km of the surface, which is consistent with our interpretation of at least a thin lithospheric mantle lid beneath the northern plateau. Upwelling of the asthenosphere would provide a source of heat to partially melt the remaining mantle lithosphere, and the long history of subduction beneath the southern margin of Asia could provide the hydrous material needed to lower the melting point of the lithosphere in the north. Still, the ability of such a process to produce the coherent shear wave anisotropy is not clear to us despite the clear spatial association of large splitting and the deep low-velocity body. Shear heating is an attractive alternative to convective solutions for the dilemma posed by the northern plateau in that it can lead more naturally to large shear wave anisotropy in the lithosphere. It has been previously questioned as a viable mechanism because of the large stresses necessary to produce sufficiently high temperatures. However, with the realization that hydrous material and lower temperatures likely exist in the mantle lithosphere of the northern plateau, we believe it would be appropriate for future work on the evolution of the Tibetan Plateau to carefully reexamine the contribution that this mechanism might make in the generation of high temperatures in the northern plateau.

Acknowledgments. The authors would like to thank the many scientists and field workers who endured the hardships of field work in the Tibetan Plateau and greatly contributed to the success of this experiment. We would especially like to thank Frances Wu, whose persistence made this cooperative effort possible. Contributors included Chinese participants from the Institute of Geophysics, State Seismological Bureau, PRC, and the Seismological Bureaus of the Qinghai Province and the Tibetan Autonomous Region. U.S. participants in the field program included F. Wu (SUNY-Binghamton), R. Busby (PIC-LDGO), R. Kuehnel (Carnegie-DTM), G. Randall, G Wagner, S. Owens and M. Salvador (USC). We would like to thank A. Calderwood, M. Murphy, A. Yin, R. Ryerson, and G. Zandt for many helpful discussions. Also, careful reviews by T. Hearn, E. Sandvol, and M. Hamburger greatly improved the presentation of this work. This project was supported by NSF grants EAR-9004428, EAR-9196115, and EAR-9206815 to USC. C. Ammon received support from IGPP-LLNL grant 94-10. D. McNamara was supported by LLNL in the summer of 1994, and work was performed under the auspices of the U.S. Department of Energy by Lawrence Livermore National Laboratory under contract W-7405-ENG-48. Maps were created using GMT [*Wessel and Smith*, 1991].

References

Anderson, O. L., E. Schreiber, R. C. Liebermann, and N. Soga, *Pn* velocity variations, *Rev. Geophys., 6,* 491–524, 1968.

Arnaud, N. O., P. Vidal, P. Tapponnier, P. Matte, and M. Deng, The high K_2O volcanism of northwestern Tibet: Geochemistry and tectonic implications, *Earth Planet. Sci. Lett., 111,* 351–367, 1992.

Beghoul, N., M. Barazangi, and B. L. Isacks, Lithospheric structure of Tibet and western North America: Mechanisms of uplift and a comparative study, *J. Geophys. Res., 98,* 1997–2016, 1993.

Bourjot, L., and B. Romanowicz, Crust and upper mantle tomography in Tibet using surface waves, *Geophys. Res. Lett., 19,* 881–884, 1992.

Brandon, C., and A. Romanowicz, A "no-lid" zone in the central Chang-Thang platform of Tibet: Evidence from pure path phase velocity measurements of long-period Rayleigh waves, *J. Geophys. Res., 91,* 6547–6564, 1986.

Chapman, C. H., and J. Orcutt, The computation of body wave synthetic seismograms in laterally homogeneous media, *Rev. Geophys., 23,* 105–163, 1985.

Deng, W., A preliminary study on the petrology and petrochemistry of the Quaternary volcanic rocks of the northern Tibet Autonomous region, *Acta Geol. Sin.*, Engl. Transl., 52, 148–152, 1978.

Dewey, J. F., R. M. Shackleton, F. R. S. Chang Cheng, and S. Yiyin, The tectonic evolution of the Tibetan Plateau, *Philos. Trans. R. Soc. London, 327,* 379–413, 1988.

Durham, W. B., and C. Goetze, Plastic flow of oriented single crystals of olivine, 1, Mechanical data, *J. Geophys. Res., 82,* 5737, 1977.

Gajewski, D., R. Stangl, K. Fuchs, and K. J. Sandmeier, A new constraint on the composition of the topmost continental mantle: Anomalously different depth increases of *P* and *S* velocity, *Geophys. J. Int., 103,* 497–507, 1990.

Grand, S. P., A possible station bias in travel time measurements reported to the ISC, *Geophys. Res. Lett., 17,* 17–20, 1990.

Gupta, V., Locating nuclear explosions at the Chinese test site near Lop Nor, *Sci. Global Security, 5,* 205–244, 1995.

Harrison, T. M., P. Copeland, W. S. F. Kidd, and A. Yin, Raising Tibet, *Science, 255,* 1663–1670, 1992.

Hearn, T. M., *Pn* travel times in southern California, *J. Geophys. Res., 89,* 1843–1855, 1984.

Hearn, T. M., Anisotropic *Pn* tomography in the western United States, *J. Geophys. Res., 101,* 8403–8414, 1996.

Hearn, T. M., and R. W. Clayton, Lateral velocity variations in southern California, II, Results for the lower crust from *Pn* waves, *Bull. Seismol. Soc. Am., 76,* 511–520, 1986.

Hearn, T. M., N. Beghoul, and M. Barazangi, Tomography of the western United States from regional arrival times, *J. Geophys. Res., 96,* 16,369–16,381, 1991.

Hirahara, T., and A. Hasemi, Tomography of subduction zones using local and regional earthquakes and telesesisms, in *Seismic Tomography: Theory and Practice,* edited by H. M. Iyer and K. Hirahara, pp. 519–562, Chapman and Hall, New York, 1994.

Holt, W. E., and T. C. Wallace, Crustal thickness and upper mantle velocities in the Tibetan Plateau region from the inversion of regional *Pnl* waveforms: Evidence for a thick upper mantle lid beneath southern Tibet, *J. Geophys. Res., 95,* 12,499–12,525, 1990.

Houseman, G. A., D. P. McKenzie, and P. Molnar, Convective instability of a thickened boundary layer and its relevance for the thermal evolution of continental convergence belts, *J. Geophys. Res., 86,* 6115–6132, 1981.

Isaak, D. G., High-temperature elasticity of iron-bearing olivines, *J. Geophys. Res., 97,* 1871–1885, 1992.

Jin, Y., M. K. McNutt, and Y. Zhu, Evidence from gravity and topography data for folding of Tibet, *Nature, 371,* 669–674, 1994.

Jin, Y., M. K. McNutt, and Y. Zhu, Mapping the descent of Indian and Eurasian plates beneath the Tibetan Plateau from gravity anomalies., *J. Geophys. Res., 101,* 11,275–11,290, 1996.

Karato, S., Importance of anelasticity in the interpretation of seismic tomography, *Geophys. Res. Lett., 20,* 1623–1626, 1993.

Karato, S., and P. Wu, Rheology of the upper mantle: A synthesis, *Science, 260,* 771–778, 1993.

Lyon-Caen, H., Comparison of the upper mantle shear wave velocity structure of the Indian shield and the Tibetan Plateau and tectonic implications, *Geophys. J. R. Astron. Soc., 86,* 727–749, 1986.

McNamara, D. E., Lithospheric structure of the Tibetan Plateau, Ph.D. dissertation, 259 pp., Univ. of S.C., Columbia, 1995.

McNamara, D. E., T. J. Owens, P. G. Silver, and F. T. Wu, Shear wave

anisotropy beneath the Tibetan Plateau, *J. Geophys. Res., 99,* 13,655–13,665, 1994.

McNamara, D. E., T. J. Owens, and W. R. Walter, Observations of regional phase propagation across the Tibetan Plateau, *J. Geophys. Res., 100,* 22,215–22,229, 1995.

Molnar, P., and W. P. Chen, *S-P* travel time residuals and lateral inhomogeneity in the mantle beneath Tibet and the Himalaya, *J. Geophys. Res., 89,* 6911–6917, 1984.

Molnar, P., A review of geophysical constraints on the deep structure of the Tibetan Plateau, the Himalaya and the Karakoram, and their tectonic implications, *Trans. R. Soc. London., Ser. A, 327,* 33–88, 1988.

Molnar, P., S-wave residuals from earthquakes in the Tibetan region and lateral variations in the upper mantle, *Earth Planet. Sci. Lett., 101,* 68–77, 1990.

Molnar, P., Mantle dynamics, uplift of the Tibetan Plateau, and the Indian monsoon, *Rev. Geophys., 31,* 357–386, 1993.

Molnar, P., and W. P. Chen, Focal depths and fault plane solutions of earthquakes under the Tibetan Plateau, *J. Geophys. Res., 88,* 1180–1196, 1983.

Molnar, P., and H. Lyon-Caen, Fault plane solutions of earthquakes and active tectonics of the Tibetan Plateau and its margins, *Geophys. J. Int., 88,* 1180–1196, 1989.

Mooney, W. D., and L. W. Braile, The seismic structure of the continental crust and upper mantle of North America, in *The Geology of North America,* vol. A, *The Geology of North America—An Overview,* edited by A. W. Bally and A. R. Palmer, pp. 39-52, Geol. Soc. of Am., Boulder, olo., 1989.

Ni, J., and M. Barazangi, High frequency seismic wave propagation beneath the Indian shield, Himalayan arc, Tibetan Plateau and surrounding regions: High uppermost mantle velocities and efficient propagation beneath Tibet, *Geophys. J. R. Astron. Soc., 72,* 665–689, 1983.

Owens, T. J., G. E. Randall, F. T. Wu, and R. S. Zeng, PASSCAL instrument performance during the Tibetan Plateau passive seismic experiment, *Bull. Seismol. Soc. Am., 83,* 1959–1970, 1993.

Patton, H. J., and S. R. Taylor, *Q* structure of the Basin and Range from surface waves *J. Geophys. Res., 89,* 6929–6940, 1984.

Randall, G. E., C. J. Ammon, and T. J. Owens, Moment-tensor estimation using regional seismograms from portable network deployments, *Geophys. Res. Lett., 22,* 1665–1668, 1995.

Sato, H., I. S. Sacks, T. Murase, G. Muncill, and H. Fukuyama, Q_P melting temperature relation in peridtite at high pressure and temperature: Attenuation mechanism and implications for the mechanical properties of the upper mantle, *J. Geophys. Res., 94,* 10,647–10,661 1989.

Scheidegger, A. E., and P. L. Willmore, The use of a least squares method for the interpretation of data from seismic surveys, *Geophysics, 22,* 9–22, 1957.

Soga, N., E. Schreiber, and O. L. Anderson, Estimation of bulk modulus and sound velocities of oxides at very high temperatures, *J. Geophys. Res., 71,* 5315–5320, 1966.

Turner, S., C. Hawksworth, J. Liu, N. Rogers, S. Kelley, and P. van Calsteren, Timing of the Tibetan uplift constrained by analysis of volcanic rocks, *Nature, 364,* 50–54, 1993.

Wessel, P., and W. Smith, Free software helps map and display data, *Eos Trans. AGU, 72,* 445–446, 1991.

Wittlinger, G., F. Masson, G. Poupinet, P. Tapponnier, J. Mei, G. Herquel, J. Guilbert, U. Achauer, X. Guanqi, S. Danian, and Lithoscope Kunlun Team, Seismic tomography of northern-Tibet and Kunlun: evidence for crustal blocks and mantle velocity contrasts, *Earth Planet. Sci. Lett., 139,* 263–279, 1996.

Woodward, R. L., and P. Molnar, Lateral heterogeneity in the upper mantle and *SS-S* traveltime intervals for *SS* rays reflected from the Tibetan Plateau and its surroundings, *Earth Planet. Sci. Lett., 135,* 139–148, 1995.

Zhang, S., and S. Karato, Lattice preferred orientation of olivine aggregates deformed in simple shear, *Nature, 375,* 774–777, 1995.

Zhao, L. S., and D. V. Helmberger, Geophysical implications from relocations of Tibetan earthquakes: Hot lithosphere, *Geophys. Res. Lett., 18,* 2205–2208, 1991.

Zhao, L. S., and J. Xie, Lateral variations in compressional velocities beneath the Tibetan Plateau from *Pn* traveltime tomography, *Geophys. J. Int., 115,* 1070–1084, 1993.

Zhu, L., and D. V. Helmberger, Intermediate depth earthquakes beneath the India-Tibet collision zone, *Geophys. Res. Lett., 23,* 435–438, 1996.

Zhu, L., T. J. Owens, and G. E. Randall, Lateral variation in crustal structure of the nothern Tibetan Plateau inferred from teleseismic receiver functions, *Bull. Seismol. Soc. Am., 85,* 1531–1540, 1995.

C. J. Ammon, Department of Earth and Atmospheric Sciences, St. Louis University, St. Louis, MO 63103. (e-mail: ammon@mantle.eas.slu.edu)

D. E. McNamara and W. R. Walter, Geophysics and Global Security, Lawrence Livermore National Lab., P.O. Box 808, L-202, Livermore, CA 94551. (e-mail: dmcnamara@llnl.gov; bwalter@llnl.gov)

T. J. Owens, Department of Geological Sciences, University of South Carolina, Columbia, SC 29208. (e-mail: owens@seis.sc.edu)

(Received January 3, 1996; revised June 10, 1996;
accepted June 26, 1996.)